Combustion and Flame 162 (2015) 1265–1274

Contents lists available at ScienceDirect

Combustion and Flame

journal homepage: www.elsevier.com/locate/combustflame

Decomposition mechanisms of Cu-based oxygen carriers for chemical looping with oxygen uncoupling based on density functional theory calculations

Yongliang Zhang, Haibo Zhao *, Lei Guo, Chuguang Zheng

State Key Laboratory of Coal Combustion, Huazhong University of Science and Technology, Wuhan 430074, PR China

ARTICLE INFO

Article history:
Received 29 May 2014
Received in revised form 25 October 2014
Accepted 27 October 2014
Available online 24 November 2014

Keywords:
Density functional theory
Oxygen release mechanisms
Sintering resistance
Reactivity
Cu-based oxygen carriers
Chemical looping with oxygen uncoupling

ABSTRACT

A clear understanding of the oxygen release mechanisms of Cu-based oxygen carriers with or without supports can help rationalize the design of high performance oxygen carriers (OC) for chemical looping with oxygen uncoupling (CLOU). Using periodical density functional theory (DFT) calculations and thermogravimetric analysis (TGA) experiments, this research investigated the decomposition mechanisms of CuO, $CuAl_2O_4$ and CuO/$CuAl_2O_4$ and the effects of adding supports on the Cu-based OC performance. First, the most likely oxygen release pathway was investigated for the CuO(1 1 1) surface at different oxygen release stages (O_2 formation, O_2 desorption and O anion diffusion in slab). Atomic-level details regarding the release of oxygen from CuO in CLOU are provided. The formation and desorption of O_2 were the rate-limiting steps from both DFT calculation and experimental results, with energy barriers of 3.0 and 2.7 eV, respectively. Second, $CuAl_2O_4$ presented different oxygen release features. In this case, the O anion diffusion is largely endothermic (2.53 eV) and much greater than that of CuO (0.88 eV). Thus, the required decomposition temperature increases and the decomposition rate of $CuAl_2O_4$ decreases. Next, the sintering inhibition mechanisms of $CuAl_2O_4$ that support active CuO were clarified, and strong interactions between the Al sites and CuO clusters were observed. The Al bound to O in the CuO clusters had a shorter bond length (1.874 Å) and the adsorption of Cu_4O_4 on $CuAl_2O_4$ had a greater absorption energy (−4.25 eV), which prevented the agglomeration and growth of CuO nanoclusters. Finally, the effects of $CuAl_2O_4$ addition on CuO reactivity were studied. The interactions of CuO and $CuAl_2O_4$ resulted in the redistribution of electrons in CuO, which favored the resistance of CuO to sintering but not its reactivity.

1. Introduction

Recently, attention has been given to CO_2 emissions from fossil fuel combustion due to its contribution to global warming. Chemical-looping combustion (CLC) is a highly promising approach that allows for the inherent separation of CO_2 with low cost and energy penalties [1]. In a typical CLC process, fuel combustion is divided into two steps, the reduction of a solid oxygen carrier (OC) by the fuels and the re-oxidation of the OC by the air. This two-step reaction process avoids direct contact between the fuel and air, producing CO_2 and H_2O without N_2. However, it is difficult to use solid fuels in the conventional CLC process due to the rate-limiting gasification step of the solid fuels (e.g., coal). Recently, a novel CLC process was proposed to overcome this issue [2]. This process is called chemical looping with oxygen uncoupling (CLOU). The CLOU process takes advantage of the properties of some metal oxides that release gaseous O_2 at high temperatures (800–1000 °C). The CLOU process is divided into three reaction steps and proceeds in two interconnected fluidized bed reactors, a fuel reactor (FR) and an air reactor (AR). In the FR, gaseous O_2 is generated from the decomposition of OC and is used for fuel combustion. The reduced OC is sent to the AR and is re-oxidized by the air. The dominant reaction equations within the FR and the AR are shown below.

$$2MeO_x \rightarrow 2MeO_{x-1} + O_2 \quad \text{(Fuel reactor)} \tag{1}$$

$$\text{Fuel} + O_2 \rightarrow CO_2 + H_2O \quad \text{(Fuel reactor)} \tag{2}$$

$$2MeO_{x-1} + O_2 \rightarrow 2MeO_x \quad \text{(Air reactor)} \tag{3}$$

In the CLOU process, the gaseous oxygen released due to OC substantially facilitates a much faster conversion rate of solid fuels at the combustion temperatures of interest (800–1000 °C). To date, many materials suitable for CLOU or CLC have been tested, such as

* Corresponding author. Fax: +86 27 8754 5526.
E-mail address: klinsmannzhb@163.com (H. Zhao).

http://dx.doi.org/10.1016/j.combustflame.2014.10.018
0010-2180/

CuO/Cu_2O, Mn_2O_3/Mn_3O_4, perovskite-type oxides, copper ore [3] and synthetic materials [4–7]. Among the finite metal complexes suitable for CLOU, copper-based OC has drawn significant attention because of its high reactivity and oxygen transport capacity. Despite being the most favorable, CuO faces challenges due to its low mechanical strength and high sintering tendency, which may lead to defluidization and low reactivity in CLOU systems. Generally, CuO is supported by inert support materials, such as TiO_2, ZrO_2, Al_2O_3 and $MgAl_2O_4$ [1,5,8], which are thermally stable with a high melting point. These support materials can withstand higher temperatures (900–1000 °C). In addition, Al_2O_3 has been widely used because of its low cost and abundant reserve. Cyclic redox performance studies of Al_2O_3 stabilized Cu-based OC indicate that Al_2O_3 can substantially improve the mechanical strength of OC and limit its sintering/agglomeration [9,10]. However, when the temperature is greater than 700 °C, Al_2O_3 tends to interact with CuO to form $CuAl_2O_4$ [11]. Previous studies [5,6] have found that $CuAl_2O_4$ possesses slow oxygen release kinetics at 950–1050 °C and influences the decomposition rate of the bulk CuO by decreasing the OC activity. Song et al. [12] reported that the presence of sodium-containing species could inhibit the formation of $CuAl_2O_4$. Similarly, Quddus et al. [13] reported that Co minimized the formation of irreducible bulk nickel aluminate in NiO/Al_2O_3. Along with these authors, a study by Chuang et al. [9] suggested that the high performance of the OCs was associated with a high degree of dispersion during the stabilizing activity phase.

Although some high performance OCs have been obtained in massive trial-and-error experiments, a fundamental understanding of the oxygen release characteristics of the OC is rare. For example, the following characteristics are not understood: (i) the oxygen release pathways and corresponding activation energy barriers, which are related to the mechanisms of OC decomposition, and (ii) the electronic properties of the supported OC and the interactions between different species, which naturally determine the OC sintering resistance and reactivity. A clear understanding of these mechanisms and atomic level behaviors is useful for rational design or for optimizing the OC particles. Because the required information is rarely obtained from experiments, a density functional theory (DFT) calculation was used to investigate the chemical and physical properties of the OC at a molecular level and atomic level in this study.

DFT calculations have been successfully used to (i) determine the microscopic reaction kinetics of metal compounds, such as the hydrogen absorption/desorption features of hydrogen storage materials [14,15] and the effects of the addition of transition metals on these features [16,17], and to (ii) determine the properties (both physical and chemical) of the supported catalyst, such as the specific roles of the Al_p sites in Pt/PtO sintering over a γ-Al_2O_3 support [18] and the interactions of different catalyst species for catalytic ozonation [19]. In addition, several studies have been performed to detect the electronic properties and the atomic level behaviors of OC for CLC using DFT calculations. Li et al. [20] found that the improved reactivity of TiO_2 supported iron oxide particles that most likely resulted from the significantly enhanced O^{2-} diffusivity in the presence of support. This finding was verified by the Pt marker experiment. Accordingly, these researchers [21] suggested that the mixed ionic–electronic conductive (MIEC) supported OC was more effective for CLC because it enabled fast solid state O^{2-} and electron/hole exchange between the iron oxide nanocrystallites and the OC particle surface. Previously, Siriwardane et al. [22] investigated the molecular orbital interactions between carbon (C6) and CuO (Cu_2O_2) using the DFT method. These authors found that when carbon approached the CuO molecules, the Cu–O bond was elongated and contributed to breaking the Cu–O bond, which was prone to the CLC reaction. Qin et al. [23] studied the synergetic effects of Al_2O_3, ZrO_2 and MgO on Fe_2O_3 for the CLC of CO. These authors demonstrated that these supports could activate Fe_2O_3 for oxidizing CO into CO_2 and reduce the barrier energy in the following order: $Fe_2O_3 > Fe_2O_3/Al_2O_3 > Fe_2O_3/MgO > Fe_2O_3/ZrO_2$. However, the underlying mechanisms of CuO decomposition, the sintering inhibition mechanisms of the supports and the effects of the supports on the reactivity of Cu-based OC have not been comprehensively studied.

In this study, we investigated the CuO and $CuAl_2O_4$ decomposition mechanisms to identify the rate-limiting steps of oxygen release and to explore the oxygen release features. Next, the interactions between the $CuAl_2O_4$ and the CuO nanoclusters were studied to clarify the role of the supports in determining the sintering resistance and reactivity of CuO. Both temperature programmed decomposition (TPD) and isothermal oxygen release experiments of sol–gel Cu-based OCs were conducted in a thermogravimetric analyzer (TGA) to relate the DFT calculation with experimental observations. The calculated predictions agreed with the experimental results very well and gave an insight on the Cu-based OC decomposition features. A brief discussion of the effects of preparation method and support addition on the reactivity of the OC was also given. These results may motivate researchers to understand the O_2 release features of Cu-based OC in CLOU and prompt rational OC design or optimization.

2. Experimental and computational details

OC preparation methods mainly include impregnation, mechanical mixing, spray drying, and so on [1]. To date, only spray drying material has been successfully tested in a CLOU unit [24,25]. However, the distribution of CuO is non-uniform and the strength between CuO and support is not very high in the OC particles prepared by these methods, which is disadvantageous for increasing the content of CuO or the integrity of the particle. The OCs used in this study were prepared by the sol–gel method [26,27]. The closely mixed of CuO and support at molecular level can be reached in this technique, ensuring the fully contact between CuO phase and $CuAl_2O_4$ phase. The characteristic is consistent with the DFT model using in this work, in which the $CuO/CuAl_2O_4$ model is periodic and the components are fully in contact with each other.

A detailed description of the sol–gel preparation steps of the method has been discussed previously [28,29]. Aluminum isopropoxide ($Al(OC_3H_7)_3$) and $Cu(NO_3)_2{\cdot}6H_2O$ were used as precursors. After stepwise drying in air at 100–600 °C, the samples were calcined at 1050 °C. After crushed and screened, three OCs with sizes of 125–180 μm were obtained, including pure CuO, $CuO/CuAl_2O_4$ (wt. 30%/70%) and $CuAl_2O_4$, with stoichiometrically molar Cu and Al ratios.

To study the reactivity and oxygen release characteristic of these OCs, TPD and isothermal experiments were performed using thermogravimetric analysis (TGA). The samples were fully oxidized at relatively lower temperature in air before using. In TPD experiments, thirty milligrams of OC were heated from room temperature to 1000 °C under a N_2 flow of 100 mL/min and at a heating rate of 10 °C/min. In isothermal experiments, thirty milligrams of OC were first heated from room temperature to 900 °C and 1000 °C under an air flow of 100 mL/min, respectively. When the temperature was stable, the atmosphere was switched to a N_2 flow of 100 mL/min. Oxygen release and uptake of CuO/Cu_2O for 20 cycles was also conducted. It was performed at 900 °C under a N_2 atmosphere in oxygen release period and under an air atmosphere in oxygen uptake period. The sample weight and the reaction temperature were recorded continuously during the TGA experiment.

The fresh and used OCs were analyzed using a powder X-ray diffraction instrument (Shimadzu, XRD-7000) with Cu Kα radiation and 2θ = 10–90°. For this instrument, the maximum tube voltage

was 40 kV and the maximum current was 30 mA. The phase analyses of the fresh and used OCs are listed in Table 1. These results revealed the presence of small concentrations of CuO and Al_2O_3 in the fresh $CuAl_2O_4$ OC, which indicated that some of the CuO and Al_2O_3 did not convert to $CuAl_2O_4$. Furthermore, no Al_2O_3 was found in the fresh $CuO/CuAl_2O_4$ OC due to the excess CuO in this OC. The results also revealed that the conversion of CuO to Cu_2O and the conversion of $CuAl_2O_4$ to $CuAlO_2$ or Al_2O_3 occurred in the oxygen release process. Small amounts of $CuAl_2O_4$ existed in the used OCs due to the incomplete decomposition.

The DFT calculations were performed using the nonlocal generalized gradient approximation (GGA) function by employing the Perdew–Wang (PW91) [30,31] correlation functional in CASTEP (Cambridge Serial Total Energy Package) [32]. The CuO unit cell adopts a monoclinic structure (*C2/c* space group) [33], in which each Cu atom bonds with four O atoms (see Fig. 1a) and the $CuAl_2O_4$ unit cell adopts a cubic structure (*Fd/3m* space group) [34], as shown in Fig. 1d. A cubic Cu_4O_4 nanocluster (see Fig. 1b) was built to simulate the active phase that adhered to the support. Periodic boundary conditions were applied to these unit cells across all three dimensions. The CuO cluster was optimized in a large cubic box of 20 Å × 20 Å × 20 Å to eliminate the periodicity effects.

The Brillouin zone integrations were performed using Monkhorst–Pack type mesh [35], and an antiferromagnetic spin ordering was used for the CuO unit cell [33,36]. Before structure optimization, convergence tests of the energy cutoff (4 points from 300 to 450 eV) and the k-points separation (4 points from 0.06 to 0.03 $Å^{-1}$) were performed. An energy cutoff of 400 eV and a k-points separation of 0.04 resulted in well-converged total structure energies that were within 0.02 eV of each other and could be neglected. To accurately describe the strong electron correlations in transition-metals, the Hubbard parameter (U) was introduced for the Cu 3d orbitals according to the well-known GGA + U method [37]. We tested the DFT + U with U from 0 to 9 eV and found that using U = 7.5 eV for the Cu 3d orbitals provided reasonable results. In addition, this value was suggested by previous researchers [33,38]. Thus, we applied U = 7.5 eV to the Cu 3d orbitals throughout this paper. The calculated Cu–O bond lengths of the CuO cluster (1.952 Å) and the CuO unit cell (1.956 Å) agreed with the experimental data (1.95 Å) [39]. In addition, the calculated lattice parameter for the $CuAl_2O_4$ was $a = b = c$ = 8.158058 Å, which was comparable to other calculation [34] and experimental results [40].

The CuO(1 1 1) surface was used to study the oxygen release characteristics of CuO. This surface was selected because it is the most stable low-index CuO surface that contains compact Cu–O layers under ambient conditions, as discussed by [33] and [36]. Similarly, $CuAl_2O_4$(1 0 0) [41] was selected for this study. The CuO(1 1 1) (see Fig. 1c) and $CuAl_2O_4$(1 0 0) surfaces (see Fig. 1e) were cleaved from the CuO and $CuAl_2O_4$ unit cell, respectively. Three-layer (2 × 2) CuO(1 1 1) (containing 48 atoms) and (1 × 2) $CuAl_2O_4$(1 0 0) slabs (containing 42 atoms) were built, which converged to a surface energy of within 0.005 and 0.018 J/m^2. A vacuum gap of 20 Å was used above the surface to prevent slab–slab interactions. Subsequently, the CuO(1 1 1) and $CuAl_2O_4$(1 0 0) surfaces were fully relaxed until the threshold values of energy, displacement and force were reached (0.01 meV, 0.001 Å and 0.03 eV/Å, respectively) when the bottom layer was fixed. These convergence criteria were used throughout the paper. The calculated surface energy of the CuO(1 1 1) was 0.71 J/m^2, which was comparable to the earlier calculation results of 0.72 J/m^2 [36] and 0.74 J/m^2 [33].

Table 1
Compositions of the fresh and the used OCs.

	Fresh	After oxygen release
CuO	CuO	Cu_2O
$CuO/CuAl_2O_4$	CuO and $CuAl_2O_4$	Cu_2O, $CuAlO_2$, Al_2O_3 and $CuAl_2O_4^m$
$CuAl_2O_4$	$CuAl_2O_4$, $Al_2O_3^m$ and CuO^m	$CuAlO_2$, Al_2O_3 and $CuAl_2O_4^m$

m = Minor phase.

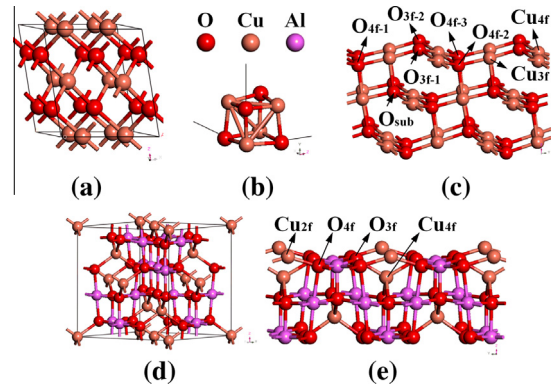

Fig. 1. (a) CuO unit cell, (b) Cu_4O_4 cluster, and (c) CuO(1 1 1) slab with different types of Cu and O atoms, (d) $CuAl_2O_4$ unit cell, and (e) $CuAl_2O_4$(1 0 0) slab with different types of Cu and O atoms.

The CuO nanoclusters that were supported on the surface systems were calculated using the periodic supercell of the $CuAl_2O_4$ support slab and the same calculation setup to ensure consistency between the calculations. The adsorption energy (E_{ad}) of the CuO nanoclusters on the supports is defined as

$$E_{ad} = E(Cu_4O_4/CuAl) - [E(CuAl) + E(Cu_4O_4)] \quad (4)$$

where E(CuAl) and $E(Cu_4O_4)$ are the total energies of the bare $CuAl_2O_4$ surface and the free Cu_4O_4 cluster and $E(Cu_4O_4/CuAl)$ is the total energy of the Cu_4O_4 cluster supported on the $CuAl_2O_4$ surface. E_{ad} reflects the stability of the cluster supported on the surface. A negative adsorption energy indicates that the structure is more stable than a separated cluster and surface [42].

In this study, the complete LST/QST approach (linear/quadratic synchronous transit) [43] was used to find transition state (TS) structures and to determine the energy barriers (E_b) of different oxygen release steps. The value of E_b was calculated as follows:

$$E_b = E(TS) - E(IS) \quad (5)$$

where E(TS) and E(IS) are the energies of the TS and the initial states (IS), respectively.

3. Oxygen release mechanisms of CuO

3.1. OC decomposition behavior by experiments

Before conducting detailed DFT calculations, we have performed OC decomposition experiments at isothermal conditions. Decomposition rate at different conversion of OC were obtained from the experiments. The experimental observations help to outline the decomposition mechanism.

The TG curves of CuO decomposition in different CLOU cycles at 900 °C were shown in Fig. 2. It was found that the mass loss of CuO after the reaction was about 10%, suggesting the CuO had been fully converted to Cu_2O. Figure 3 showed that the CuO can be also fully converted to Cu_2O at different isothermal conditions (900 °C and 1000 °C). The oxygen release rates of these particles as a function of OC conversion were presented in Fig. 4. Factually, the XRD results showed that only Cu_2O phase was detected in the used CuO OC, as shown in Table 1. Thus, not only the O anions in the outer layers of the CuO, but also the O anions in the internal layer of

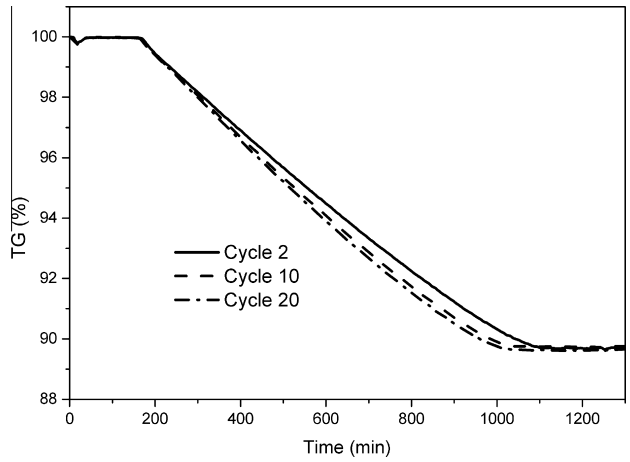

Fig. 2. Mass loss of the CuO in different CLOU cycles at 900 °C in N_2 flow as a function of time.

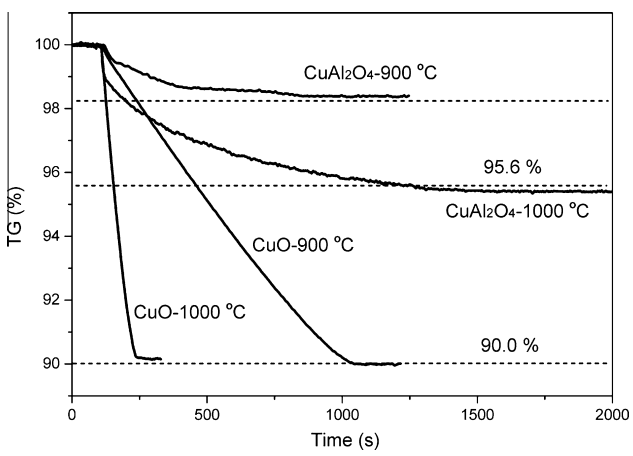

Fig. 3. Mass loss of CuO and $CuAl_2O_4$ in N_2 flow at 900 °C and 1000 °C as a function of time, respectively, 95.6% meaning that $CuAl_2O_4$ has been fully decomposed to $CuAlO_2$, and 90% meaning that CuO has been fully decomposed to Cu_2O.

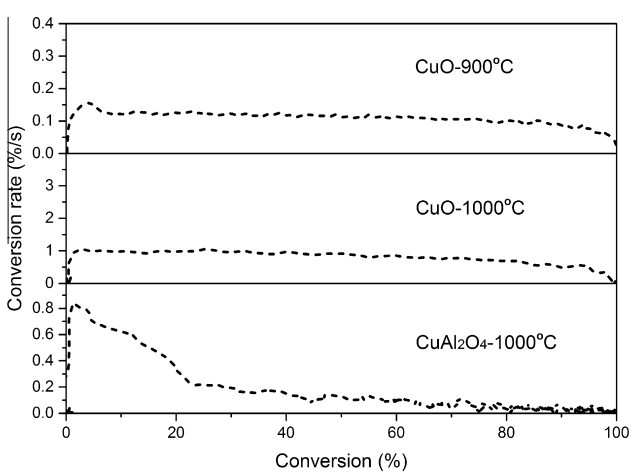

Fig. 4. Oxygen release rate (conversion rate) of CuO and $CuAl_2O_4$ decomposition at 900 °C and 1000 °C as a function of conversion.

the CuO participate in the oxygen release. Therefore, it is reasonably deduced that the O_2 release of CuO is related to the internal O anion diffusion and the O_2 formation and desorption. Previous study showed that the decomposition process of H_2 storage materials [15,44,45] or "hercynite cycle" active materials [46] included similar steps, such as gas formation, desorption and anion diffusion. It is a reasonable simplified assumption that O_2 formation, O_2 desorption and O anion diffusion steps are included in the oxygen release of CuO.

The effect of CuO particle structure (which will determine the outward diffusion of desorbed O_2 molecule from the micropores within the OC particles) on the oxygen release rate of the CuO was examined. After cyclic oxygen release and uptake processes, the BET surface and pore volumes of the CuO will be reduced because of slight sintering. However, from Fig. 2, it was found that the oxygen release rate had little changes after 10 and 20 cycles. This suggested that the O_2 molecule diffusion outside from the pores has little effect on the oxygen release rate, compared to the CuO decomposition reaction (including of O_2 formation, O_2 desorption and O anion diffusion). Therefore, only steps of O_2 formation (S1), O_2 desorption (S2) and O anion diffusion (S3) were considered in the work.

The details of the isolate steps in the CuO decomposition process help to gain insight on CuO decomposition mechanism, which is hardly detected by experiments. To further elaborate on the key features of OC decomposition and identify the rate limiting steps, DFT was used to investigate the oxygen release details of the CuO(1 1 1) surface model. We first focused on the most reasonable pathways for O_2 formation and desorption on the CuO surface and investigated the diffusivity of the subsurface O anion.

3.2. The formation and desorption of oxygen on the CuO(1 1 1) surface

Figure 1c showed the relaxed atomic structure of a pure CuO(1 1 1) surface. On the surface, four chemically distinguishable types of surface atoms were labeled, Cu_{3f} as the three fold-coordinated Cu atoms, Cu_{4f} as the four fold-coordinated Cu atoms, O_{3f} as the three fold-coordinated O atoms and O_{4f} as the four fold-coordinated O atoms. The O_{3f} were more exposed on the surface relative to the O_{4f}, which were coordinated with a Cu_{3f} atom and two Cu_{4f} atoms. In addition, the O_{4f} atoms were coordinated with three surface Cu atoms and a subsurface Cu atom, which limited their migration. Thus, in high temperature environments, the O_{3f} atoms can migrate more easily than the O_{4f} atoms.

To determine the possible O_2 formation process (S1), an O_{3f} atom was removed and reintroduced to bond with four adjacent O atoms, including O_{3f-2}, O_{4f-1}, O_{4f-2} and O_{4f-3} (see Fig. 1c). Next, these structures were optimized. The O_{3f} atoms cannot bond with the O_{4f-2} and O_{4f-3} atoms. Instead, the O_{3f} atoms form bonds with the O_{3f-2} and O_{4f-1} atoms (with bond lengths of 1.523 and 1.429 Å, respectively). These bond lengths were slightly longer than the bond lengths of the free O_2 molecules (1.225 Å), which indicated that an O_2 complex was formed in the two structures. Furthermore, the reconstructed structures with O_{3f-1}–O_{3f-2} and O_{3f-1}–O_{4f-1} complexes on the surfaces had lower surface energies, which implied that they were thermodynamic stable and easily formed. Thus, the O_2 formation processes of O_{3f-1}–O_{3f-2} and O_{3f-1}–O_{4f-1} were investigated and denoted by P1 and P2, respectively. Figure 5 shows the two investigated pathways, beginning with the perfect CuO(1 1 1) surface (initial state, donated by IS) and ending with the CuO(1 1 1) surface with the formation of O_2 complexes (intermediate state, donated by IM). Next, a TS (transition-state) search calculation was performed to identify the TS structure and the corresponding energy barrier (see Fig. 6). These results showed that the energy barrier was 2.3 eV for P1–S1 and 3.0 eV for P2–S1. In addition, the reaction energies were 2.1 eV and 2.5 eV, respectively. These findings suggested that bonding was more likely between O_{3f-1} and O_{3f-2}. Next, we continued the calculation to investigate the S2 process.

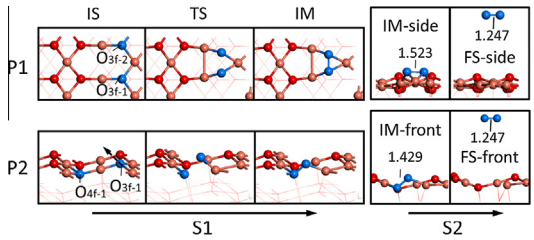

Fig. 5. The initial state (IS), transition state (TS), intermediate state (IM) and final state (FS) structures for the O_2 formation (S1) and O_2 desorption (S2) processes in different pathways (P1 and P2) on the CuO(1 1 1) surface. The IM-side and IM-front are the side and front views of the IM structure, respectively. The FS-side and FS-front are the side and front views of the FS structure, respectively. The highlighted blue O atoms are the same atoms in the IS structures for P1 and P2, respectively. The bond lengths are presented in Å. (For interpretation of the references to color in this figure legend, the reader is referred to the web version of this article.)

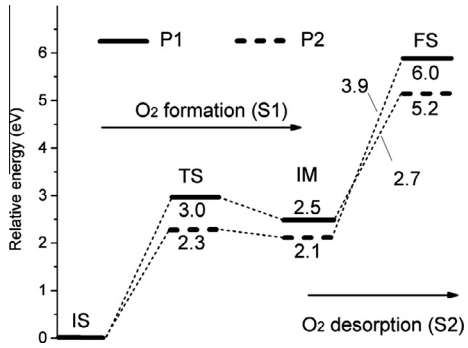

Fig. 6. Potential energy diagram for the O_2 formation and O_2 desorption processes following different pathways (P1 and P2) and on the CuO(1 1 1) surface.

O_{3f-1}–O_{4f} and O_{3f-1}–O_{3f-2} (in the IM of P1 and P2) were removed from the surface before placing at a distance of 6 Å from the CuO(1 1 1) surface. Next, the structures were optimized and denoted by the FS (final state) of P1 and P2 (see Fig. 5). There, the IS can be labeled as $(CuO)_x$, and the FS can be labeled as O_2(a free molecule) + Cu_xO_{x-2}(reduced CuO). After this step, a TS search calculation was performed to obtain the energy barrier from the IM to the FS. We observed that the energy barriers were nearly equal to the reaction energies and that the values are high for the P1–S2 and P2–S2 processes (3.9 eV for P1–S2 and 2.7 eV for P2–S2). Once an O_2 complex was formed on the surface, a high thermodynamic driving force was required for it to enter the gas phase.

The potential energy diagram suggested that (as shown in Fig. 6) the P1 and P2 processes were largely endothermic, which implied that oxygen release only occurs at high temperatures (greater than 800 °C according to the thermodynamic calculation [2]). In addition, the highest energy barrier of P2 was 3.0 eV, which was much lower than that of P1 (3.9 eV). Moreover, the FS of P2 was more thermodynamically stable than that of P1 due to its lower total energy. Therefore, P2 was regarded as the most favorable pathway for the formation of O_2 and for the desorption on the CuO(1 1 1) surface. In the P2 process, two bonds between the O_{3f-1} and Cu_{4f} atoms break and the O_{3f-1} migrates from the initial site to the top of the Cu_{3f} (see the TS of P2 in Fig. 5) before binding to the O_{4f-1}. Meanwhile the Cu_{3f} atom binds to the two adjacent Cu_{4f} atoms and the energy barrier is 3.0 eV. After an O_2 complex is formed on the surface, a desorption energy of 2.7 eV is required to rupture the Cu–O bond and allow the O_2 to enter the gas phase. In the FS of P2, the O_2 has a bond length of 1.247 Å, which is similar to the bond lengths in free O_2 molecules (1.225 Å).

To understand the key state of the P2 process, we determined the electronic structures of the free O_2 molecules and the O_{3f-1} and O_{4f} atoms in the IS, IM and FS. The local density of states (LDOS) of these structures are plotted in Fig. 7. In the IS, a large delocalization of the p orbitals occurs for the two O atoms, which resulted from the strong Cu–O bonds in the CuO. In the IM, a clear splitting of the O_{3f-1} and O_{4f} s orbitals was observed. Two small peaks appeared in the energy region of −23 eV and −16 eV, which indicated that the formation of O–O complexes occurred in the IM. Meanwhile, the p orbitals near 0 eV became slightly small, which indicated that the O–O complex transferred some electrons to the surface and still had strong interactions with the surface. In the FS, the two small peaks were split in the energy region of −26 eV and −14 eV, which indicated that the O–O bond became stronger. Meanwhile, the p orbitals decreased to large spikes, indicating that the O–O complex transferred some electrons to the surface again and the interactions between the O–O complex and the surface was much weak. The LDOS of the O_2 in the FS corresponded with that of the free O_2 molecules, which indicated that free molecular O_2 was formed.

3.3. The diffusion of the O anion from lattice to surface in the CuO slab

CuO decomposition depends on the formation (S1) and desorption (S2) of the surface O_2 and on the outward diffusion of the O anion in the CuO slab (S3). The diffusivity mechanism of the O anion in the CuO slab after the S1 and S2 processes was further investigated.

For this calculation, we used the CuO(1 1 1) structure with a surface O_{3f} vacancy (denoted as V_{O3f}) of IS and the CuO(1 1 1) structure with a subsurface O_{sub} vacancy (denoted as V_{Osub}) of FS. In addition, O_{sub} was the nearest O atom to O_{3f}. The IS and FS structures were optimized before performing the calculation. Figure 8 shows the TS search results and the corresponding energy barrier of the S3 process. As shown in Fig. 8, when beginning with a surface vacancy in the IS, the O_{sub} atom migrates from the initial site to the middle position between the surface and subsurface O vacancies. In addition, the O_{sub}–Cu bond in the subsurface is gradually ruptured (see TS in Fig. 8). Next, the O_{sub} atom binds to the surface Cu atoms before occupying the V_{O3f} (see FS in Fig. 8). The reaction energy of the S3 process is negative (−0.70 eV), which indicates that the process is exothermic and energetically favorable. The calculated energy barrier of the S3 process is 0.88 eV, which is significantly lower than that of the S1 (3.0 eV) and S2 (2.7 eV) processes. This energy barrier occurs because only one Cu–O bond in the S3

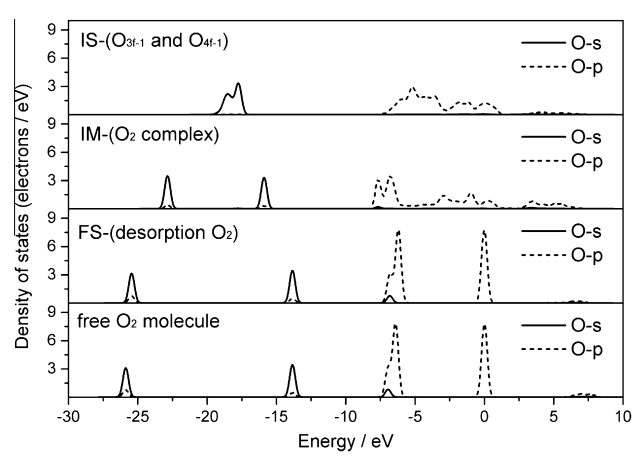

Fig. 7. Local density of states for the O_{3f-1} and O_{4f} atoms in the IS, IM and FS during the O_2 formation (S1) and O_2 desorption (S2) processes and the local density of states for the free O_2 molecules.

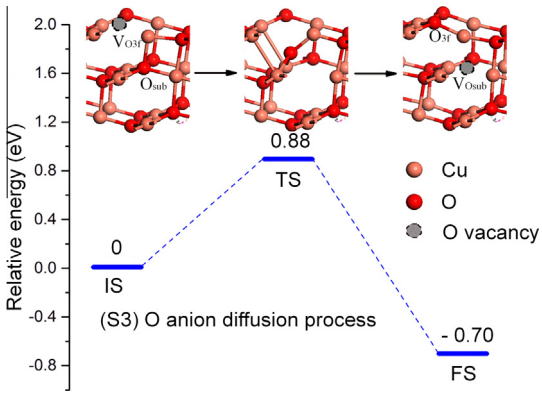

Fig. 8. The structures of the initial states (IS), transition states (TS) and final states (FS) for O anion diffusion in the CuO slab and the corresponding potential energy diagram.

process is broken from the IS to the TS. However, in the S1 and S2 processes, at least two Cu–O bonds must be broken. The diffusion energy barriers of the deeper layer O anions are also relatively low due to the diffusion features of the deeper layer O anions are similar to those of the subsurface O anion, where only one Cu–O bond is broken from the IS to TS.

Based on our calculations, we determined the most favorable oxygen release pathway. First, the surface O atom migrates and forms O_2 complexes at the surface with an energy barrier of 3.0 eV. Next, the O_2 complex is desorbed from the surface and enters the gas phase with an energy barrier of 2.7 eV. As O vacancies are created in the surface, the subsurface O anions migrate outward to fill the vacancies with a relatively low energy barrier of 0.88 eV. The O anions migrate from the deeper slab layer to provide surface O atoms for the following oxygen release steps. The driving force results from the high temperature and low partial pressure of oxygen. Figure 9 shows a schematic representation for the CuO oxygen release system, in which the formation (S1 process) and desorption (S2 process) of O_2 leaves some O vacancies at the CuO surface. These O vacancies facilitate the migration of the O anion from the subsurface to the surface (S3 process).

In the oxygen release process, the formation and desorption of O_2 are more rate-limiting than the anion diffusion of O inside the CuO slab due to their higher energy barriers. CuO decomposition experiments also supported the DFT results. Figure 4 shows the oxygen release rates (conversion rates) of CuO at 900 °C and 1000 °C. It was found that the oxygen release rate was about 0.1%/s at 900 °C and about 1.0%/s at 1000 °C, where the oxygen release rates had little changes at different conversion. It means that sufficient O anions always exist in the CuO crystal surface at different conversion to supply the O_2 formation and desorption. If the O anion diffusion is a rate limiting step for the CuO decomposition, the oxygen release rate will be significantly reduced, because the mobility distance of O anion from internal lattice to

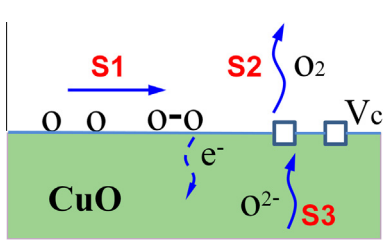

Fig. 9. A schematic representation for the CuO oxygen release mechanism. The arrows indicate the trends of the various species.

the surface is longer and the O anion diffusion occurs more frequently at a higher conversion. Therefore, the O anion diffusion may be not a rate limiting rate for oxygen release of CuO. This is consistent with the calculation prediction. In addition, the activation energies of CuO oxygen release that were measured in previous studies [47,48] were 322.2 kJ/mol (3.34 eV) and 327 kJ/mol (3.39 eV) for particle sizes of 10 μm and between 1 and 10 μm, respectively. The calculated energy barriers for O_2 formation (3.0 eV) and desorption (2.7 eV) are comparable to the experimental activation energies. The experimental data reflect the entire oxygen release process of CuO, including the formation of O_2 at the surface, the desorption of O_2 from the surface and the diffusion of O anion in the CuO slab. Thus, a difference exists between the energy barrier and the experimental activation energy. However, the experiment provides a baseline for the calculation.

It is interesting to find ways to improve the reactivity and stability of OC. The energy barriers have a close relationship with the reactivity of OC. Thus, one method for improving the reactivity is to reduce these energy barriers for different steps, especially for the S1 and S2 steps, to facilitate oxygen release. Another method is to increase the surface area of the active CuO to provide more sites for the formation and desorption of O_2 while decreasing the distance of O diffusion. For the OC of CuO, several support materials (such as $CuAl_2O_4$) have been used to limit sintering and maintain the surface area. However, previous experiments [6] have shown that Cu-based OCs with different supports present various reactivities at similar surface areas and pore volumes. This result suggests that the support addition influences the surface area of the CuO and the oxygen release features of the CuO, such as the energy barriers of O_2 formation, O_2 desorption or O anion diffusion. A clear understanding of the interaction mechanisms of the CuO with the support is highly desirable for rationalizing the design of high performance OC.

4. Interactions between the support and the CuO

4.1. Oxygen release characteristics of $CuAl_2O_4$ by experiments

Previous studies [5,6] have reported that the $CuAl_2O_4$ does not release oxygen in an inert atmosphere at 900–925 °C. However, when the temperature is greater than 950 °C, $CuAl_2O_4$ follows a slow decomposition mechanism. The oxygen release characteristics of $CuAl_2O_4$ were investigated before using it as the CuO support. First, OC decomposition experiments at isothermal conditions (900 °C and 1000 °C) were carried out and the results were shown in Figs. 3 and 4.

In Fig. 3, for the $CuAl_2O_4$ material, the mass loss is 1.6% at 900 °C and about 4.5% at 1000 °C, suggesting at 900 °C, only the CuO phase in the $CuAl_2O_4$ material participates in decomposition, but at 1000 °C, both the $CuAl_2O_4$ and CuO phases participate in decomposition, at a relatively higher temperature. Figure 4 shows the conversion rate at different conversion of the $CuAl_2O_4$ and CuO, and it can be seen clearly that the CuO phase is decomposed much faster than $CuAl_2O_4$ phase at 1000 °C. In addition, as noticed, the conversion rate of $CuAl_2O_4$ is obviously reduced in higher conversion periods, which is different from that of CuO, indicating the $CuAl_2O_4$ has different decomposition features with CuO.

We also performed a TPD experiment to determine the different oxygen release features of CuO and $CuAl_2O_4$. Figure 10 shows the mass loss as a function of temperature in the TGA for CuO, CuO/$CuAl_2O_4$ and $CuAl_2O_4$. The pure CuO is rapidly decomposed in one step, and the decomposition begins at approximately 800 °C. However, CuO/$CuAl_2O_4$ and $CuAl_2O_4$ are decomposed in two steps. The small concentration of CuO species that exist in the fresh $CuAl_2O_4$ OC and the large concentrations of CuO that exist in the fresh CuO/$CuAl_2O_4$ OC result in rapid conversion rates at

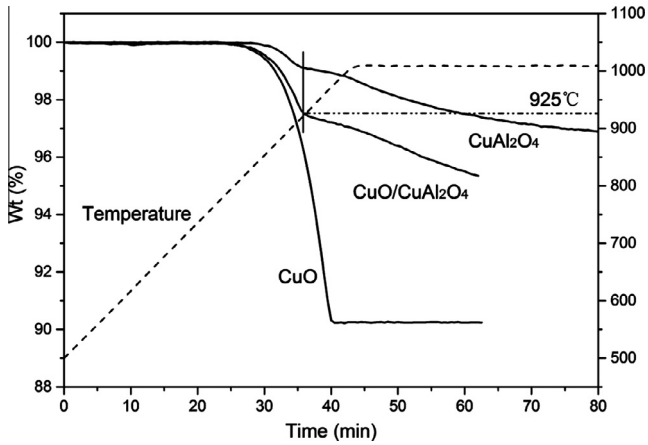

Fig. 10. TPD profiles of pure CuO, $CuAl_2O_4$ and CuO/$CuAl_2O_4$ (wt. 30%/70%). The solid vertical line corresponds to the temperatures at which the weight loss has a significant change.

temperature lower than 925 °C. When the temperature reaches more than 925 °C, a very slow conversion rate occurs for CuO/$CuAl_2O_4$ and $CuAl_2O_4$, which results from the $CuAl_2O_4$ phase decomposition. The TPD results also indicate that the $CuAl_2O_4$ has a higher decomposition temperature and a slower conversion rate, which is consistent with the isothermal experiments and the previous experiment results [5,49].

4.2. Detailed oxygen release mechanism of $CuAl_2O_4$

Next, DFT calculation was performed to further elaborate the oxygen release features of the $CuAl_2O_4$. In this calculation, different oxygen release pathways were tested. The pathway with the lowest energy barriers was discussed here. As shown in Fig. 11, in the O_2 formation process (S1), the threefold coordinated O atoms (O_{3f}) that bind with the fourfold coordinated Cu atoms (Cu_{4f}) break the two Al–O bonds and make bond with another O_{3f} at the other Cu sites. The bond length of the O–O bond in the IM structure (Fig. 11c) is 1.499 Å. In the O_2 desorption process (S2), the resulting O_2 complex breaks the bonds with the surface to escape into the gas phase with a bond length of 1.254 Å. The S1 and S2 processes lead to the reconstruction of the surface. When the O_2 has been desorbed, the surface is made of Cu–O–Al rings (Fig. 11d). In the O diffusion process (S3) from the IS to the TS, as shown in Fig. 11e and f, the subsurface O breaks one of the Cu–O bonds and two of the Al–O bonds to bind with the surface Cu and Al atoms.

The calculated reaction energy of S3 (from IS to FS) equals the energy barrier (from IS to TS), which reaches up to 2.53 eV. Thus, this process is largely endothermic and is ascribed to the compact structure of the $CuAl_2O_4$. This process is significantly different from the diffusion of the O anion in CuO, which is exothermic with reaction energy of −0.70 eV. According to thermodynamics, the diffusion of O from $CuAl_2O_4$ is more difficult and requires a higher oxygen release temperature. The energy barriers of the oxygen release steps for $CuAl_2O_4$ and CuO are plotted in Fig. 12. Although the energy barriers of S1 and S2 are comparable between the two materials, the energy barriers for $CuAl_2O_4$ in S3 were much higher than for CuO and the value is close to the energy barriers of S1 and S2. This difference indicates that S3 is also a rate limiting steps for $CuAl_2O_4$ decomposition besides S1 and S2, and it will reduce the oxygen release rate (conversion rate) of $CuAl_2O_4$. These DFT calculation results agree well the isothermal and TPD experiments shown in Figs. 3, 4 and 10, which suggest that $CuAl_2O_4$ has a higher decomposition temperature and a slower conversion rate. In higher conversion periods of $CuAl_2O_4$, S3 occurs frequently and will become the dominant step for oxygen release. Therefore, the DFT calculation explains the reason why $CuAl_2O_4$ shows different oxygen release features with CuO.

4.3. Sintering inhibition mechanism of $CuAl_2O_4$ in the Cu-based OC

CuO sintering diminishes the surface area for the formation and desorption of O_2 and elongates the diffusion pathway of the O anion, which deteriorates the OC reactivity. Previous studies [5,6,9,10,12,29] have indicated that $CuAl_2O_4$ can efficiently limit CuO sintering and have suggested that the stable reactivity of the OCs is associated with a high degree of CuO dispersion in the particle. The actual OC particles with a high degree of CuO dispersion can be simplified as the adhesion of the CuO nanocluster to the $CuAl_2O_4$ grain. We used a model of Cu_4O_4 nanoclusters supported

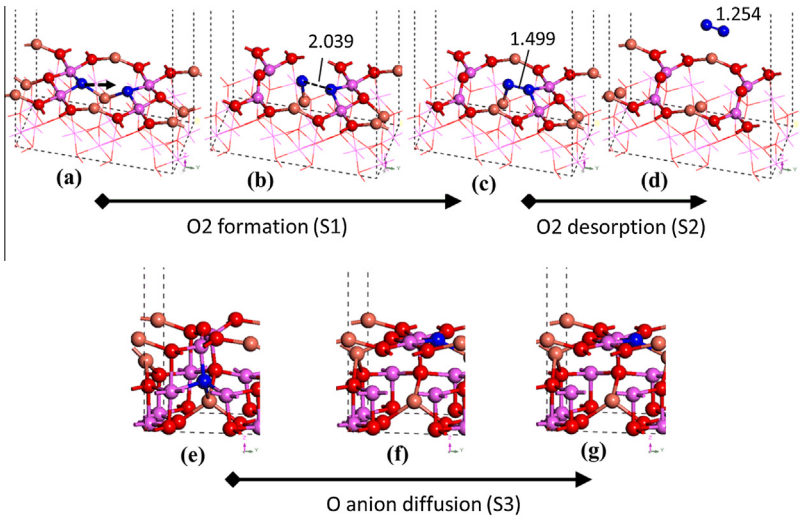

Fig. 11. The structures of the (a) IS – initial states, (b) TS – transition states, (c) IM – intermediate states, and (d) FS – final states for the S1 – O_2 formation process and the S2 – O_2 desorption process on the $CuAl_2O_4$(100) surface. In addition, the structures of (e) IS – initial states, (f) TS – transition states and (g) FS – final states for the S3 – O anion formation process. The highlighted blue O atoms are the same atoms represented in the IS structures for P1 and P2, respectively. The bond lengths are presented in Å. (For interpretation of the references to color in this figure legend, the reader is referred to the web version of this article.)

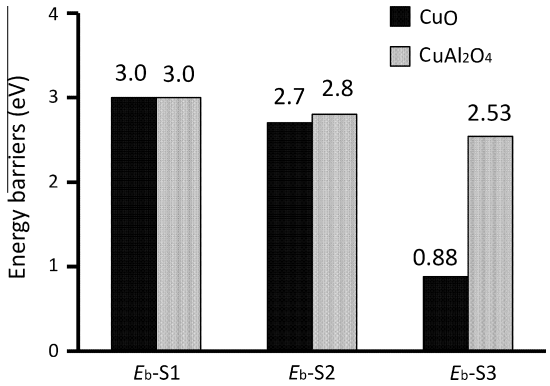

Fig. 12. Energy barriers of the different oxygen release steps (the S1 – O_2 formation process, S2 – O_2 desorption process and S3 – O anion formation process) for CuO and $CuAl_2O_4$.

on the $CuAl_2O_4$ surface to perform this calculation. The CuO and $CuAl_2O_4$ are fully in contact with each other in the periodic model structure and the model can describe the structures of sol–gel OC particles.

First, the Cu_4O_4 nanocluster was added to the $CuAl_2O_4$(100) surface and then was optimized. Figure 13a shows the atomic structure of the Cu_4O_4 supported on $CuAl_2O_4$(100), where four new bonds are formed between the cluster and the surface. Two Cu atoms from the cluster make bonds with the two surface O atoms, and the two O atoms from the cluster bind with the two surface Al atoms, while the Cu_4O_4 maintains its cubic structure. In addition, we have determined that the Cu_4O_4 nanoclusters are supported on the CuO surface (see Fig. 13d). Five new bonds were formed between the cluster and the CuO(111) surfaces, but the structure of the Cu_4O_4 tends to be disordered. The lengths of the new bonds between the surface and cluster are listed in Table 2. From Table 2, the Al_s–O_c has much shorter bond lengths (1.874 Å) relative to the new Cu–O bonds in both models. From the difference electron densities of the CuO/$CuAl_2O_4$ structures (see Fig. 10b and c), we observed a distinct charge accumulation between the surface Al and the cluster of O atoms, which indicated that a strong interaction occurred between them. This strong interaction can limit the migration of the CuO nanocluster, which implies that the Al sites on the $CuAl_2O_4$ surface play important roles in the interactions of CuO and $CuAl_2O_4$.

The adsorption energies of the Cu_4O_4 nanoclusters on the $CuAl_2O_4$ and CuO surfaces were calculated (−4.25 eV and −2.92 eV, respectively). Compared to the pure CuO surface, the $CuAl_2O_4$ as a support resulted in more negative adsorption energy. This finding mainly resulted from the effects of the Al sites on the

Table 2
The bond lengths of the newly formed bonds in the Cu_4O_4 supported on $CuAl_2O_4$(100) and the Cu_4O_4 supported on CuO(111). O^c and Cu^c correspond to the O and Cu atoms in the CuO cluster. Al^s, Cu^s and O^s are the corresponding atoms at the CuO and $CuAl_2O_4$ surfaces.

	CuO/$CuAl_2O_4$(100)	CuO/CuO(111)
O^c–Al^s/Cu^s (Å)	1.874/1.874	2.165/1.950/1.950
Cu^c–O^s (Å)	1.899/1.900	1.898/1.897

$CuAl_2O_4$ surface. In addition, the disorder of the CuO cluster structure on the CuO surface (see Fig. 13d) reduce the adsorption energy of the pure CuO surface by increasing the energy of the cluster/CuO(111). Regarding the pure CuO surface, aggregation and growth of small CuO nanoclusters may occur on the surface and lead to CuO sintering. However, the aggregation of these clusters was prevented when using $CuAl_2O_4$ because the more negative adsorption energy of the $CuAl_2O_4$ surface limited the migration of the CuO nanoclusters and provided them with stability. This result was confirmed by the experimental results [50,51], which indicated that pure CuO became compact after multiple CLC or CLOU cycles due to sintering, however, which was not observed when $CuAl_2O_4$ was added. Thus, we can use the adsorption energy of the active phase to assess the sintering resistance characteristics of the support and to select suitable supports for different OCs. In addition, it can be deduced that sufficient CuO contact with the supports favors the role of the support. Thus, a high degree of CuO dispersion or supports is required for high performance OCs. In addition, Xu et al. [52] used the surface energy of support materials to access the interactions of the active CuO and support. The lowest calculated surface energies of the $CuAl_2O_4$ and CuO were 1.38 and 0.71 J/m^2, respectively. The $CuAl_2O_4$ had a higher surface energy than the TiO_2 (0.86 J/m^2), Al_2O_3 (0.90 J/m^2) and MgO (0.87 J/m^2) [52]. Thus, the $CuAl_2O_4$ provides a higher resistance to CuO sintering than other supports.

4.4. The effect of $CuAl_2O_4$ on CuO reactivity

From Fig. 13b and c, the support causes significant electron redistribution in the CuO nanocluster, which affects the oxygen release features of the CuO. In addition, the TPD results in Fig. 10 show that the reactivity of the CuO species decreased in the CuO/$CuAl_2O_4$ OC and was more distinct for the CuO in the $CuAl_2O_4$ OC. In addition, previous studies [8] have found that high $MgAl_2O_4$ or $CuAl_2O_4$ concentrations reduce the reactivity of CuO. The support addition generally shortens the diffusion pathway of O anion in the CuO slab, which can enhance the diffusivity of the O anions. Thus, the reactivity deterioration is more likely related to the

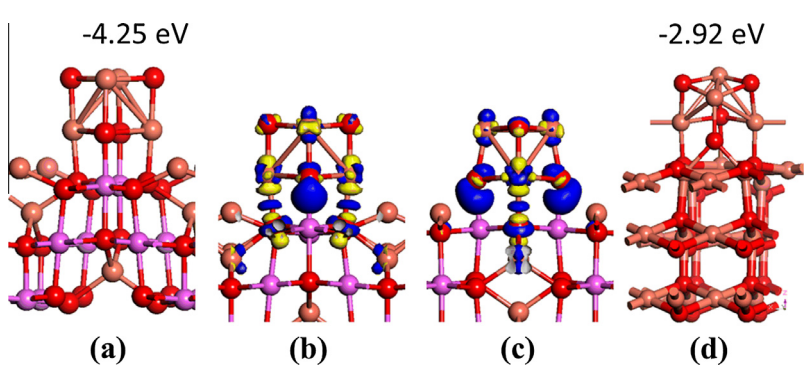

Fig. 13. The atomic structures of (a) the Cu_4O_4 supported on $CuAl_2O_4$(100) and (d) the Cu_4O_4 supported on CuO(111). Front view (b) and side view (c) of the calculated electron density difference for the Cu_4O_4 supported on $CuAl_2O_4$(100). The blue and yellow isosurfaces represent the charge gain and depletion, respectively, with an electron density difference of 0.05 e/Å^3. (For interpretation of the references to color in this figure legend, the reader is referred to the web version of this article.)

effects of the $CuAl_2O_4$ support on the O_2 formation (S1) and desorption (S2) processes during oxygen release. The oxygen release features of the CuO nanoclusters on the $CuAl_2O_4$ surface were investigated.

Figure 14 shows the O_2 formation and desorption processes of the $CuAl_2O_4$ supported CuO. Starting from the CuO/$CuAl_2O_4$ structure, the two exposed O atoms of the Cu_4O_4 cluster (O_{s-1} and O_{s-2}) break two Cu–O bonds with an energy barrier of 2.21 eV and approach each other (see the TS structure in Fig. 14). The chemisorbed O_2 complex is formed. Next in S2 process, the O_2 complex escapes the cluster gradually and remains a Cu_4O_2 cluster at the surface with an energy barrier of 3.28 eV. The energy barriers of O_2 formation (S1) and desorption (S2) for $CuAl_2O_4$ supported CuO are compared to that of the free Cu_4O_4 cluster and pure CuO surface, as shown in Fig. 15.

Figure 15 shows that the free CuO nanoclusters presents different oxygen release features than the CuO surface. In S1, the Cu_4O_4 has a much lower energy barrier of O_2 formation, mainly because the O anions in the nanocluster can migrate more easily than the compact CuO crystal surface. In S2, the Cu_4O_4 has a relatively higher energy barrier. Thus, for the CuO nanoclusters, the O_2 desorption is the rate-limiting step. The energy barrier of O_2 formation for Cu_4O_4 increases when $CuAl_2O_4$ is used as support. This increase results from the electron redistribution and structural changes of the CuO nanoclusters at the $CuAl_2O_4$ surface. The broken Cu–O bonds in Cu_4O_4/$CuAl_2O_4$ are only 1.866 Å, which are much shorter than those of Cu_4O_4 (1.952 Å). Meanwhile, the energy barrier of O_2 desorption is comparable to that of the free Cu_4O_4 and is much higher than that of the CuO surface. Thus, the $CuAl_2O_4$ supported CuO shows unfavorable oxygen release features relative to the free CuO nanoclusters and the CuO surface. This finding is consistent with the experimental results, which indicates that CuO has a relatively slower oxygen release rate, as shown in Fig. 10. The distinct reduced reactivity of OC with a high $CuAl_2O_4$ content occurred because there were less bulk CuO phases or free CuO nanoclusters in it. This result suggests that the support content in the OC particles should be maintained at a relative low level to ensure the reactivity of the OC.

As known, particles prepared by spray drying, impregnation, or other methods may have different CuO distribution on the support, resulting in different reactivities of the OC. For instance, in impregnated OC particles, the CuO component covers the support material and the CuO crystallite size is larger. Although the $CuAl_2O_4$ phase is possibly formed in the outer layer of the support, it is difficult to reach the uniform distribution of CuO and $CuAl_2O_4$ in the particles, which makes the contacts of CuO and $CuAl_2O_4$ insufficient. Thus, the effects of $CuAl_2O_4$ in impregnated materials on the CuO is relatively weak compared to the sol–gel materials. Because, as

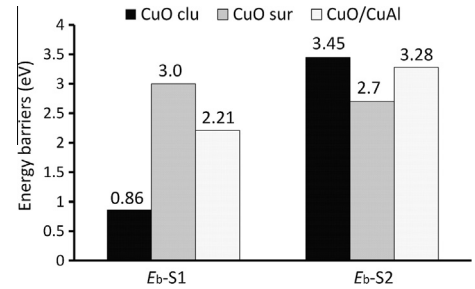

Fig. 15. Energy barriers of O_2 formation (S1) and O_2 desorption (S2) for the free Cu_4O_4 cluster, pure CuO surface and $CuAl_2O_4$ supported CuO.

revealed by the DFT calculations, the unsupported CuO is more reactive when compared with the supported one, it can be reasonably deduced that the impregnated materials will be more reactive than sol–gel material. For spray drying materials, it possesses uniform structure with CuO and support being separately distributed. The binding strength between CuO and support could be not very high, which also favors the reactivity but is disadvantageous for the integrity of the particle. To summarize, the reactivity and the sintering resistance of the OC depend on the OC structures, including CuO crystallite size, distribution and its interaction strength with the support. Suitable preparation method could give favorable CLOU performance of OC. It should be noted that Although the addition of $CuAl_2O_4$ and fully mixed of CuO and $CuAl_2O_4$ could reduce the reactivity of CuO, it maintains the reactivity of CuO in multiple CLOU cycles by preventing sintering. Different supports can result in different CuO oxygen release features and provide an opportunity for us to optimize OC in terms of reactivity maintenance and sintering inhibition.

5. Conclusions

A comprehensive study of the characteristics of Cu-based OC was performed in this study using the DFT method and TGA experiments. The CuO decomposition mechanism, the sintering inhibition mechanism of supports and the effects of the supports on the Cu-based OC reactivity were investigated at an atomic level. The major results are summarized as follows.

(i) Oxygen release mechanisms were explored at an atomic level and the most likely oxygen release pathway for the CuO(1 1 1) surface was obtained. The formation and desorption processes of O_2 were the rate-limiting steps for CuO decomposition, which is agreement with the experimental results.

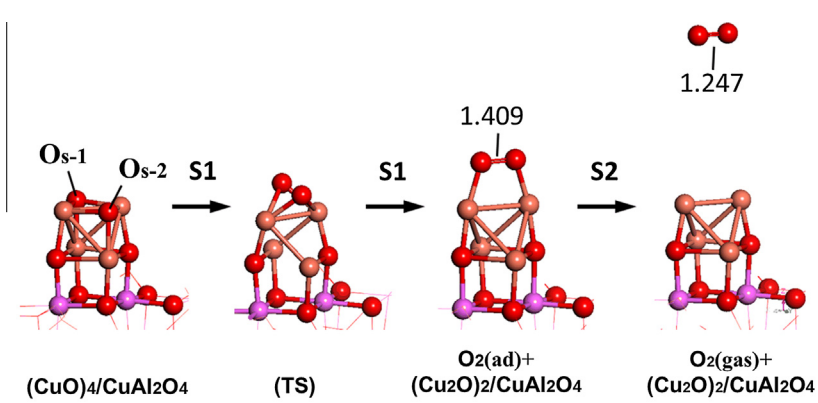

Fig. 14. The structures of the IS – initial states, TS – transition states, IM – intermediate states and FS – final states for the O_2 formation and O_2 desorption processes of $CuAl_2O_4$ supported CuO.

(ii) Isothermal and TPD experiments showed that $CuAl_2O_4$ had different oxygen release features with the CuO. The DFT results suggested that the energy barrier of O anion diffusion in the $CuAl_2O_4$ was significant higher than that in CuO and the process was largely endothermic, which decreased the oxygen release rates and increased the required oxygen release temperature of $CuAl_2O_4$.

(iii) The sites of Al at the $CuAl_2O_4$ surface played important roles in limiting the sintering of CuO. The adsorption energy of Cu_4O_4 on $CuAl_2O_4$ was −4.25 eV higher than that of Cu_4O_4 on the pure CuO (−2.92 eV). The adsorption energy can be used to assess the interactions of different species in OC particles and the sintering inhibition characteristics of the supports.

(iv) The desorption of O_2 is the only rate-limiting step for oxygen release from the CuO nanoclusters, which is different from the oxygen release features of the CuO surface. The interactions of CuO and $CuAl_2O_4$ result in electron redistribution at the CuO supported on $CuAl_2O_4$ surfaces, which does not favor CuO reactivity. The $CuAl_2O_4$ content in the OC should be maintained at a relatively low level while ensuring the sintering inhibition of the OC.

In conclusion, good agreement was obtained between the DFT calculations and the oxygen release experiments of sol–gel OCs. And these results will help us elucidate the characteristics of Cu-based OC. Additional research is required to optimize the $CuO/CuAl_2O_4$ OC and to select OCs with higher performance.

Acknowledgments

This research was funded by the "National Natural Science Foundation of China (51390494)" and "National Key Basic Research and Development Program" (2011CB707300).

References

[1] J. Adanez, A. Abad, F. Garcia-Labiano, P. Gayan, L.F. de Diego, Prog. Energy Combust. Sci. 38 (2) (2012) 215–282.
[2] T. Mattisson, A. Lyngfelt, H. Leion, Int. J. Greenhouse Gas Control 3 (1) (2009) 11–19.
[3] H. Zhao, K. Wang, Y. Fang, J. Ma, D. Mei, C. Zheng, Int. J. Greenhouse Gas Control 22 (2014) 154–164.
[4] W. Yang, H. Zhao, J. Ma, D. Mei, C. Zheng, Energy Fuels 28 (2014) 3970–3981.
[5] M. Arjmand, A.-M. Azad, H. Leion, A. Lyngfelt, T. Mattisson, Energy Fuels 25 (11) (2011) 5493–5502.
[6] Q. Imtiaz, M. Broda, C.R. Müller, Appl. Energy 119 (C) (2014) 557–565.
[7] W. Yang, H. Zhao, K. Wang, C. Zheng, Proc. Combust. Inst. (2014), http://dx.doi.org/10.1016/j.proci.2014.07.010.
[8] P. Gayán, I. Adánez-Rubio, A. Abad, L.F. de Diego, F. García-Labiano, J. Adánez, Fuel 96 (2012) 226–238.
[9] S. Chuang, J. Dennis, A. Hayhurst, S. Scott, Combust. Flame 154 (1) (2008) 109–121.
[10] Q. Imtiaz, A.M. Kierzkowska, M. Broda, C.R. Müller, Environ. Sci. Technol. 46 (6) (2012) 3561–3566.
[11] M.-F. Luo, P. Fang, M. He, Y.-L. Xie, J. Mol. Catal. A: Chem. 239 (1–2) (2005) 243–248.
[12] Q. Song, W. Liu, C.D. Bohn, R.N. Harper, E. Sivaniah, S.A. Scott, J.S. Dennis, Energy Environ. Sci. 6 (1) (2013) 288–298.
[13] M.R. Quddus, M.M. Hossain, H.I. de Lasa, Catal. Today 210 (2013) 124–134.
[14] R.W. Wagemans, J.H. van Lenthe, P.E. de Jongh, A.J. van Dillen, K.P. de Jong, J. Am. Chem. Soc. 127 (47) (2005) 16675–16680.
[15] A. Du, S.C. Smith, X. Yao, G. Lu, Surf. Sci. 600 (9) (2006) 1854–1859.
[16] A. Du, S.C. Smith, X. Yao, G. Lu, J. Am. Chem. Soc. 129 (33) (2007) 10201–10204.
[17] L.-L. Wang, D.D. Johnson, J. Phys. Chem. C 116 (14) (2012) 7874–7878.
[18] D. Mei, J.H. Kwak, J. Hu, S.J. Cho, J. Szanyi, L.F. Allard, C.H. Peden, J. Phys. Chem. Lett. 1 (18) (2010) 2688–2691.
[19] W. Qin, X. Li, J. Qi, Langmuir 25 (14) (2009) 8001–8011.
[20] F. Li, S. Luo, Z. Sun, X. Bao, L.-S. Fan, Energy Environ. Sci. 4 (9) (2011) 3661–3667.
[21] N.L. Galinsky, Y. Huang, A. Shafiefarhood, F. Li, ACS Sustain. Chem. Eng. 1 (3) (2013) 364–373.
[22] R. Siriwardane, H. Tian, D. Miller, G. Richards, T. Simonyi, J. Poston, Combust. Flame 157 (11) (2010) 2198–2208.
[23] W. Qin, Y. Wang, C. Dong, J. Zhang, Q. Chen, Y. Yang, Appl. Surf. Sci. 282 (2013) 718–723.
[24] A. Abad, I. Adánez-Rubio, P. Gayán, F. García-Labiano, L.F. de Diego, J. Adánez, Int. J. Greenhouse Gas Control 6 (2012) 189–200.
[25] I. Adánez-Rubio, A. Abad, P. Gayán, L. de Diego, F. García-Labiano, J. Adánez, Int. J. Greenhouse Gas Control 12 (2013) 430–440.
[26] C.J. Brinker, G.W. Scherer, Sol-Gel Science: The Physics and Chemistry of Sol-Gel Processing, Academic Press, 1990.
[27] D. Mei, A. Abad, H. Zhao, J. Adanez, C. Zheng, Energy Fuels (2014), http://dx.doi.org/10.1021/ef501981g.
[28] H. Zhao, L. Liu, B. Wang, D. Xu, L. Jiang, C. Zheng, Energy Fuels 22 (2) (2008) 898–905.
[29] D. Mei, H. Zhao, Z. Ma, C. Zheng, Energy Fuels 27 (5) (2013) 2723–2731.
[30] J.P. Perdew, J. Chevary, S. Vosko, K.A. Jackson, M.R. Pederson, D. Singh, C. Fiolhais, Phys. Rev. B 46 (11) (1992) 6671.
[31] J.P. Perdew, K. Burke, M. Ernzerhof, Phys. Rev. Lett. 77 (18) (1996) 3865.
[32] M. Segall, P.J. Lindan, M. Probert, C. Pickard, P. Hasnip, S. Clark, M. Payne, J. Phys.: Condens. Matter 14 (11) (2002) 2717.
[33] J. Hu, D. Li, J.G. Lu, R. Wu, J. Phys. Chem. C 114 (40) (2010) 17120–17126.
[34] Q.-J. Liu, Z.-T. Liu, Appl. Phys. Lett. 99 (9) (2011) 091902.
[35] H.J. Monkhorst, J.D. Pack, Phys. Rev. B 13 (12) (1976) 5188–5192.
[36] Y. Maimaiti, M. Nolan, S.D. Elliott, Phys. Chem. Chem. Phys. 16 (7) (2014) 3036–3046.
[37] V.I. Anisimov, J. Zaanen, O.K. Andersen, Phys. Rev. B 44 (3) (1991) 943.
[38] D. Wu, Q. Zhang, M. Tao, Phys. Rev. B 73 (23) (2006) 235206.
[39] V. Massarotti, D. Capsoni, M. Bini, A. Altomare, A. Moliterni, Z. Kristallogr. 213 (5) (1998) 259–265.
[40] R.F. Cooley, J.S. Reed, J. Am. Ceram. Soc. 55 (8) (1972) 395–398.
[41] X. Yin, H. Han, M. Kubo, A. Miyamoto, Theor. Chem. Acc. 109 (4) (2003) 190–194.
[42] A. Iwaszuk, M. Nolan, Q. Jin, M. Fujishima, H. Tada, J. Phys. Chem. C 117 (6) (2013) 2709–2718.
[43] T.A. Halgren, W.N. Lipscomb, Chem. Phys. Lett. 49 (2) (1977) 225–232.
[44] K.-C. Chou, Q. Li, Q. Lin, L.-J. Jiang, K.-D. Xu, Int. J. Hydrogen Energy 30 (3) (2005) 301–309.
[45] A. Du, S.C. Smith, G. Lu, J. Phys. Chem. C 111 (23) (2007) 8360–8365.
[46] C.L. Muhich, B.W. Evanko, K.C. Weston, P. Lichty, X. Liang, J. Martinek, C.B. Musgrave, A.W. Weimer, Science 341 (6145) (2013) 540–542.
[47] D. Chadda, J.D. Ford, M. Fahim, Int. J. Energy Res. 13 (1) (1989) 63–73.
[48] E. Eyring, G. Konya, J. Lighty, A. Sahir, A. Sarofim, K. Whitty, Oil Gas Sci. Technol. – Rev. d'IFP Energies nouvelles 66 (2) (2011) 209–221.
[49] M. Arjmand, A.-M. Azad, H. Leion, T. Mattisson, A. Lyngfelt, Ind. Eng. Chem. Res. 51 (43) (2012) 13924–13934.
[50] L.F. de Diego, F. García-Labiano, J. Adánez, P. Gayán, A. Abad, B.M. Corbella, J. María Palacios, Fuel 83 (13) (2004) 1749–1757.
[51] M. Alipour, J.A. Nychka, R. Gupta, Energy Fuels (2013).
[52] L. Xu, J. Wang, Z. Li, N. Cai, Energy Fuels 27 (3) (2013) 1522–1530.